Geophysical Prospecting, 2000, **48**, 231–256

An electromagnetic modelling tool for the detection of hydrocarbons in the subsoil[1]

J.M. Carcione[2,3] and G. Seriani[2]

Abstract

Electromagnetic geophysical methods, such as ground-penetrating radar (GPR), have proved to be optimal tools for detecting and mapping near-surface contaminants. GPR has the capability of mapping the location of hydrocarbon pools on the basis of contrasts in the effective permittivity and conductivity of the subsoil. At radar frequencies (50 MHz to 1 GHz), hydrocarbons have a relative permittivity ranging from 2 to 30, compared with a permittivity for water of 80. Moreover, their conductivity ranges from zero to 10 mS/m, against values of 200 mS/m and more for salt water. These differences indicate that water/hydrocarbon interfaces in a porous medium are electromagnetically 'visible'. In order to quantify the hydrocarbon saturation we developed a model for the electromagnetic properties of a subsoil composed of sand and clay/silt, and partially saturated with air, water and hydrocarbon. A self-similar theory is used for the sandy component and a transversely isotropic constitutive equation for the shaly component, which is assumed to possess a laminated structure. The model is first verified with experimental data and then used to obtain the properties of soils partially saturated with methanol and aviation gasoline. Finally, a GPR forward-modelling method computes the radargrams of a typical hydrocarbon spill, illustrating the sensitivity of the technique to the type of pore-fluid. The model and the simulation algorithm provide an interpretation methodology to distinguish different pore-fluids and to quantify their degree of saturation.

Introduction

A typical hydrocarbon spill in the subsurface consists of various components (Schwille 1967). As can be appreciated in Fig. 1, a capillary fringe and a gaseous zone develop above the water table, and the product core is, in general, located near the water table, with a diffusion region below. Hydrocarbons do not disperse in a homogeneous way, since they form a partially dissolved phase mixed with air (gas) and water, as a consequence of rainfall, seasonal variations and the hydrogeological conditions in the area. Ground-penetrating radar (GPR) has the capability of mapping

[1] Received May 1998, revision accepted August 1999.
[2] Osservatorio Geofisico Sperimentale, PO Box 2011, Opicina, 34016 Trieste, Italy.
[3] E-mail: jcarcione@ogs.trieste.it

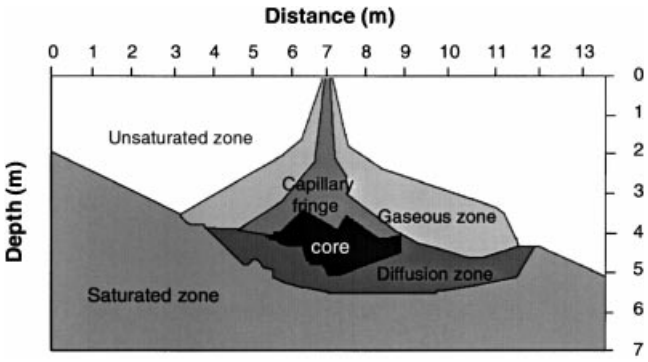

Figure 1. Model of a hydrocarbon spill. The capillary fringe for the hydrocarbon and water, and the gaseous zones are above the water table. The product core is at the water table and the diffusion zone is below the water table (after Schwille 1967; see also Daniels *et al.* 1995).

the location of the hydrocarbon spill on the basis of the dielectrical and electrical parameters (Benson 1995; Daniels, Roberts and Vendl 1995; Grumman and Daniels 1995; Nash, Atekwana and Sauck 1997; Whiteley 1997). In fact, at radar frequencies, hydrocarbons have, in general, lower permittivity and conductivity than groundwater. Subsurface features such as soil/soil (sand/clay) and unsaturated/saturated interfaces can be identified and the geometrical features of the floating hydrocarbons can be mapped with the GPR technique. Detection is based on the permittivity and conductivity contrasts between the hydrocarbon, the groundwater and the host material. At radar frequencies we may neglect interfacial and electrochemical mechanisms, such as the surface effects associated with the rock/water interface. These mechanisms are important at low frequencies and preclude the use of composite theoretical models based on a dry rock matrix (Olhoeft 1987; Knight and Endres 1990).

Few theoretical models have been proposed to describe contaminant fluid behaviour and its effects on GPR response, although Endres and Redman (1993) developed a pore-scale fluid model for clay-free granular soils. In order to predict and interpret the characteristics of the hydrocarbon spill, we develop a model for the complex permittivity of a soil composed of sand grains, clay and silt, partially saturated with gas (air), water and hydrocarbon. The theory is based on the self-similar model (Sen, Scala and Cohen 1981) for obtaining the properties of the sandy component, and a laminated transversely isotropic model for describing the shaly component of the soil. The self-similar theory guarantees the continuity of the water-filled pore space, in agreement with Archie's law (Archie 1942). On the other hand, the laminated model can be represented by a network of capacitances connected in series and in parallel, and yields, respectively, the complex dielectric constants of a partially saturated shale parallel and normal to the bedding plane (see Bergman 1978). In this case, a connectivity parameter simulates a lenticular textural pattern of the saturating fluids. This modification allows the continuity of the clay/silt matrix along the horizontal and

vertical directions. The self-similar model is used to obtain the permittivity tensor of the soil, where the shaly component is the inclusion in the homogeneous sandy matrix. The host proportion is given by the amount of quartz relative to the total solid content.

The physics of wave propagation is illustrated by probing the medium with a uniform plane wave. The analysis gives the expressions of measurable quantities, such as the energy velocity and the quality factor, as a function of propagation direction and frequency. Finally, a full-wave simulation algorithm, based on a grid method, provides the means for computing radargrams of realistic models of hydrocarbon contaminated soils. The constitutive model, together with the forward-modelling code, constitute an interpretation tool for the detection of hydrocarbon pools.

Basic constitutive relationships

The total current vector in an electromagnetic medium is the sum of the displacement currents $-\mathrm{i}\omega\boldsymbol{\epsilon}\cdot\mathbf{E}$ and the conduction currents $\boldsymbol{\sigma}\cdot\mathbf{E}$, where ω is the angular frequency, $\boldsymbol{\epsilon}(\omega)$ is the complex permittivity tensor, $\boldsymbol{\sigma}(\omega)$ is the complex conductivity tensor, and $\mathbf{E}(\omega)$ is the electric field. The constitutive relationship is given by

$$\mathbf{J} = \boldsymbol{\sigma}^* \cdot \mathbf{E}, \qquad \boldsymbol{\sigma}^* = \boldsymbol{\sigma} - \mathrm{i}\omega\boldsymbol{\epsilon}. \tag{1}$$

Alternatively, the corresponding permittivity tensor can be defined as

$$\boldsymbol{\epsilon}^* = \boldsymbol{\epsilon} + \frac{\mathrm{i}}{\omega}\boldsymbol{\sigma}. \tag{2}$$

The complex permittivity ϵ of a clean sand saturated with N constituents is obtained in Appendix A. If the subscripts q and w denote quartz and water, the complex permittivity of the composite can be obtained from the following expression:

$$\int_{\epsilon_{\mathrm{w}}^*}^{\epsilon} \frac{\mathrm{d}\epsilon'}{3\epsilon'} \left(\sum_k \eta_k \frac{\epsilon_k^* - \epsilon'}{\epsilon_k^* + 2\epsilon'} \right)^{-1} = -\ln(1-\gamma_{\mathrm{q}}), \tag{3}$$

where $\eta_k = \gamma_k/\gamma_1$, with γ_k, $k = 1, \ldots, N$ being the volume proportions of the constituents embedded in water (index 1 corresponds to quartz). For two constituents, say quartz and water, (3) reduces to

$$\left(\frac{\epsilon_{\mathrm{q}}^* - \epsilon}{\epsilon_{\mathrm{q}}^* - \epsilon_{\mathrm{w}}^*}\right)\left(\frac{\epsilon_{\mathrm{w}}^*}{\epsilon}\right)^{1/3} = \phi, \tag{4}$$

where ϕ is the rock porosity.

Moreover, we obtain in Appendix B the equation for a layered medium, where each single layer is isotropic, homogeneous and thin compared with the wavelength of the electromagnetic wave (equation (B2)). Assuming that the layer interfaces are parallel to the (x, z)-plane we obtain the complex conductivity matrix. The corresponding

permittivity matrix of the composite is given by

$$\begin{pmatrix} \epsilon_{\mathrm{T}} & 0 & 0 \\ 0 & \epsilon_{\mathrm{T}} & 0 \\ 0 & 0 & \epsilon_{\mathrm{N}} \end{pmatrix}, \tag{5}$$

where ϵ_{T} and ϵ_{N}, the transverse and normal permittivities, are given by

$$\epsilon_{\mathrm{T}} = \sum_{i=1}^{m} p_i \epsilon_i^*, \qquad \epsilon_{\mathrm{N}} = \left(\sum_{i=1}^{m} \frac{p_i}{\epsilon_i^*} \right)^{-1}, \tag{6}$$

for m isotropic single constituents, each with a proportion p_i, $i = 1, \ldots, m$.

The soil model

The model simulates the electromagnetic properties of a soil made of quartz grains and clay/silt, and partially saturated with air (gas), water and hydrocarbon. We consider that the presence of clay/silt induces anisotropy, i.e. the larger the clay content, the larger the degree of anisotropy. We assume that the clay minerals are platy and develop a stratified pattern. In fact, in some of the cores extracted near an oil refinery (a contaminated site under study, see the Acknowledgements), we observed that the flaky clay wraps around the quartz and silt grains, showing an orientated (stratified) texture.

Let us denote the respective proportions of the soil constituents by ϕ_{q} (quartz), ϕ_{cs} (clay/silt), ϕ_{a} (air), ϕ_{w} (water) and ϕ_{c} (contaminant), and the complex permittivities by ϵ_{q}^*, ϵ_{cs}^*, ϵ_{a}^*, ϵ_{w}^* and ϵ_{c}^*. We obtain the properties of the soil in three steps:

1 Equation (3) is used to obtain the permittivity ϵ_{sand} of the sandy component of the soil: a clay-free, granular medium. The proportions are

$$\gamma_{\mathrm{a}} = \phi_{\mathrm{a}}/\Phi_{\mathrm{s}}, \qquad \gamma_{\mathrm{w}} = \phi_{\mathrm{w}}/\Phi_{\mathrm{s}}, \qquad \gamma_{\mathrm{c}} = \phi_{\mathrm{c}}/\Phi_{\mathrm{s}}, \tag{7}$$

with

$$\Phi_{\mathrm{s}} = \phi_{\mathrm{q}} + \phi_{\mathrm{a}} + \phi_{\mathrm{w}} + \phi_{\mathrm{c}}.$$

2 The shaly component of the soil is described by the laminated composite model given in (6). However, in order to make the model more realistic, we assume that the structure of the shale is transversely isotropic with the fluids having a lenticular textural pattern. This effect can be simulated by introducing a connectivity parameter δ that quantifies the continuity of the clay/silt matrix along the vertical (z) and horizontal (x) directions. A similar modification, but to the elastic stiffnesses, has been proposed by Vernik and Nur (1992) for simulating a similar lenticular pattern in source rocks.

We make use of (6) and express the shale permittivities as

$$\epsilon_{\mathrm{T,shale}} = \frac{1}{\beta_{\mathrm{cs}}} [\delta N + T(\beta_{\mathrm{cs}} - \delta)] \tag{8}$$

and

$$\epsilon_{\mathrm{N,\,shale}} = \beta_{\mathrm{cs}} \left(\frac{\beta_{\mathrm{cs}} - \delta}{N} + \frac{\delta}{T} \right)^{-1}, \tag{9}$$

where

$$T = \beta_{\mathrm{cs}} \epsilon^*_{\mathrm{cs}} + \beta_{\mathrm{a}} \epsilon^*_{\mathrm{a}} + \beta_{\mathrm{w}} \epsilon^*_{\mathrm{w}} + \beta_{\mathrm{c}} \epsilon^*_{\mathrm{c}}, \qquad N = \left(\frac{\beta_{\mathrm{cs}}}{\epsilon^*_{\mathrm{cs}}} + \frac{\beta_{\mathrm{a}}}{\epsilon^*_{\mathrm{a}}} + \frac{\beta_{\mathrm{w}}}{\epsilon^*_{\mathrm{w}}} + \frac{\beta_{\mathrm{c}}}{\epsilon^*_{\mathrm{c}}} \right)^{-1}, \tag{10}$$

with

$$\beta_{\mathrm{cs}} = \phi_{\mathrm{cs}}/\Phi_{\mathrm{c}}, \qquad \beta_{\mathrm{a}} = \phi_{\mathrm{a}}/\Phi_{\mathrm{c}}, \qquad \beta_{\mathrm{w}} = \phi_{\mathrm{w}}/\Phi_{\mathrm{c}}, \qquad \beta_{\mathrm{c}} = \phi_{\mathrm{c}}/\Phi_{\mathrm{c}} \tag{11}$$

being the saturations, and

$$\Phi_{\mathrm{c}} = \phi_{\mathrm{cs}} + \phi_{\mathrm{a}} + \phi_{\mathrm{w}} + \phi_{\mathrm{c}}.$$

In the limit $\delta = 0$, $\epsilon_{\mathrm{T,\,shale}} = T$ and $\epsilon_{\mathrm{N,\,shale}} = N$. The connectivity parameter is in the range $0 \le \delta \le \beta_{\mathrm{cs}}$. When $\delta = 0$, we obtain the permittivities of a transversely isotropic electromagnetic medium with a vertical symmetry axis, and when $\delta = \beta_{\mathrm{cs}}$, we obtain a transversely isotropic medium with a horizontal symmetry axis. In these limits, the matrix has zero vertical continuity and zero horizontal continuity, respectively.

3 Finally, the shale component is the inclusion in a sand matrix of permittivity ϵ_{sand}. The host proportion P is given by the amount of quartz relative to the total solid content. We use (4) for a two-phase composite, such that the horizontal and vertical permittivities (ϵ_{T} and ϵ_{N}) of the soil can be obtained from the following expressions:

$$\left(\frac{\epsilon_{\mathrm{T,\,shale}} - \epsilon_{\mathrm{T}}}{\epsilon_{\mathrm{T,\,shale}} - \epsilon_{\mathrm{sand}}} \right) \left(\frac{\epsilon_{\mathrm{sand}}}{\epsilon_{\mathrm{T}}} \right)^{1/3} = P, \tag{12}$$

and

$$\left(\frac{\epsilon_{\mathrm{N,\,shale}} - \epsilon_{\mathrm{N}}}{\epsilon_{\mathrm{N,\,shale}} - \epsilon_{\mathrm{sand}}} \right) \left(\frac{\epsilon_{\mathrm{sand}}}{\epsilon_{\mathrm{N}}} \right)^{1/3} = P, \tag{13}$$

where

$$P = \frac{\phi_{\mathrm{q}}}{\phi_{\mathrm{q}} + \phi_{\mathrm{cs}}}. \tag{14}$$

The soil model satisfies the following properties. When the shale component is zero, $\phi_{\mathrm{cs}} = 0$, $P = 1$, $\epsilon_{\mathrm{T}} = \epsilon_{\mathrm{N}} = \epsilon_{\mathrm{sand}}$ and the medium is isotropic. When there are no quartz grains, $\phi_{\mathrm{q}} = 0$, $P = 0$, and the medium is transversely isotropic with permittivities $\epsilon_{\mathrm{T}} = \epsilon_{\mathrm{T,\,shale}}$ and $\epsilon_{\mathrm{N}} = \epsilon_{\mathrm{N,\,shale}}$. If the porosity (fluid content) is zero, the medium is described by (4), with quartz being the host medium and clay/silt being the inclusion.

The complex dielectric properties of water and of the clay/silt matrix are described by the Cole–Cole model (Cole and Cole 1941; Taherian, Kenyon and Safinya 1990):

$$\epsilon^* = \epsilon^{\infty} + \frac{\epsilon^0 - \epsilon^{\infty}}{1 - (\mathrm{i}\omega\tau)^q} + \frac{\mathrm{i}}{\omega}\,\sigma, \tag{15}$$

where ϵ^{∞} is the optical permittivity and ϵ^0 is the static permittivity.

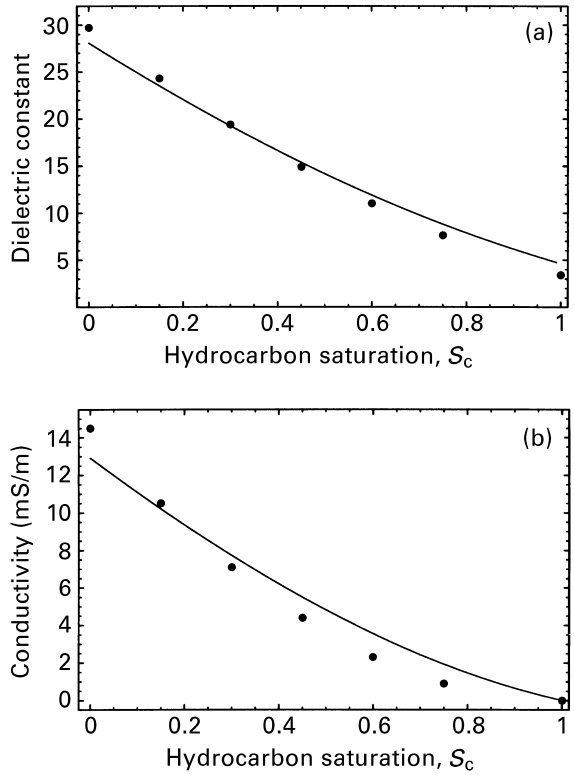

Figure 2. Comparison between the experimental and theoretical dielectric constants (a) and conductivities (b) for a water-bearing sand contaminated with perchlorethylene (PCE).

Table 1. Material properties.

Medium	ϵ (ϵ_0)	σ (S/m)
Quartz*	4.5	10^{-6}
Clay/silt	20	0.1
Air* (gas)	1	0
Rain water*	80.1	0.001
Salt water*	80.1	0.2
Methanol†	31	3×10^{-5}
Aviation gasoline†	2	10^{-6}

$\epsilon_0 = 8.85\ 10^{-12}$ F/m; $\mu_0 = 4\pi\ 10^{-7}$ H/m.
* Schön (1996); † Von Hippel (1961).

The real effective dielectric constants parallel and normal to the bedding plane are given by

$$\epsilon_{\mathrm{T,eff}} = \mathrm{Re}(\epsilon_{\mathrm{T}}), \qquad \epsilon_{\mathrm{N,eff}} = \mathrm{Re}(\epsilon_{\mathrm{N}}), \tag{16}$$

respectively, and the effective conductivities are

$$\sigma_{\mathrm{T,eff}} = \omega \mathrm{Im}(\epsilon_{\mathrm{T}}), \qquad \sigma_{\mathrm{N,eff}} = \omega \mathrm{Im}(\epsilon_{\mathrm{N}}). \tag{17}$$

Moreover, we define the formation factors $F_{\parallel}$ (parallel to the bedding plane) and $F_{\perp}$ (perpendicular to the bedding plane) as

$$F_{\parallel} = \frac{\sigma_{\mathrm{w}}}{\sigma_{\mathrm{T,eff}}}, \qquad F_{\perp} = \frac{\sigma_{\mathrm{w}}}{\sigma_{\mathrm{N,eff}}}, \tag{18}$$

where σ_{w} is related to the electrolytic conduction.

The physics of wave propagation is illustrated by probing the medium with a

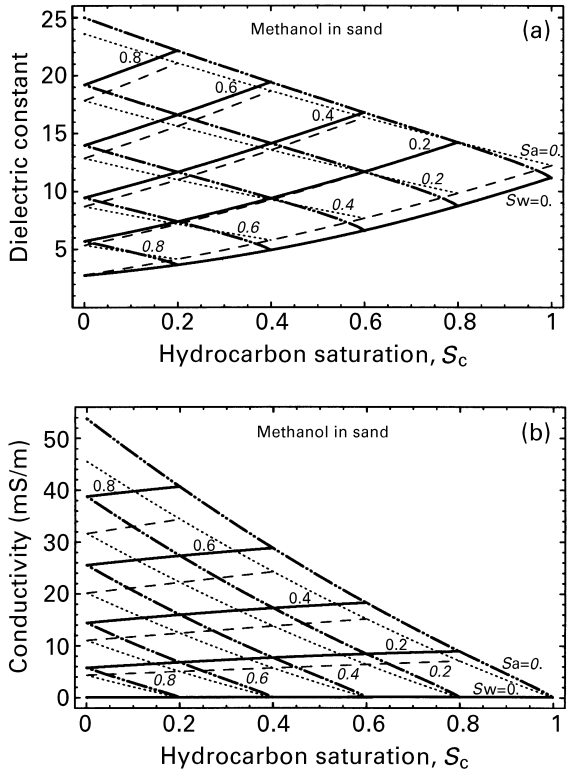

Figure 3. (a) Effective permittivity and (b) effective conductivity for sand partially saturated with methanol, water and air vs. methanol saturation. The thick continuous lines correspond to constant water saturation S_{w} (roman numbers) while the thick broken lines correspond to constant air saturation S_{a} (italic numbers). For comparison, the thin dotted and broken lines show the curves for the CRIM model.

uniform plane wave (see Appendix C). The analysis gives the expressions of measurable quantities, such as the energy velocity and the attenuation factor, as a function of propagation direction and frequency.

Examples

The sand model is tested with the results of the Borden experiment (Greenhouse *et al.* 1993; see also Schön 1996), where a water-bearing sand, with a porosity of 40%, is contaminated with perchlorethylene (PCE), classified as a DNAPL (dense non-aqueous phase liquid). We assume $\epsilon_{\rm w}^{\infty} = \epsilon_{\rm w}^{0} = 83.6\epsilon_0$, $\sigma_{\rm w} = 0.05$ S/m, $\epsilon_{\rm c} = 2.3\epsilon_0$, $\sigma_{\rm c} = 0$, $\epsilon_{\rm q} = 6.7\epsilon_0$, $\sigma_{\rm q} = 0$. The dielectric constant of quartz is assumed to be greater than the commonly tabulated value of $4.5\epsilon_0$. This takes into account the presence of electrochemical effects by considering a wetted matrix. These effects are associated with the interaction of the rock/water interface; once this has been fully established

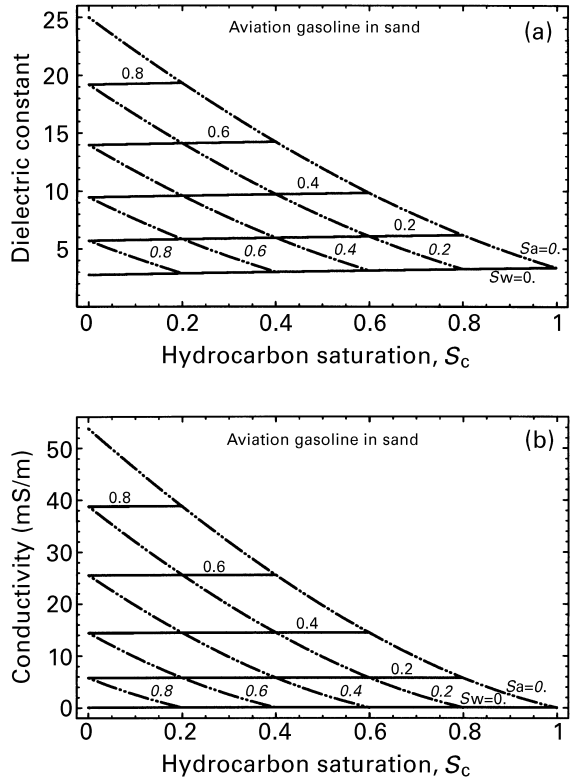

Figure 4. (a) Effective permittivity and (b) effective conductivity for sand partially saturated with aviation gasoline, water and air vs. gasoline saturation. The thick continuous lines correspond to constant water saturation $S_{\rm w}$ (roman numbers) while the thick broken lines correspond to constant air saturation $S_{\rm a}$ (italic numbers).

through the adsorption of approximately 1 nm of water, the magnitude of the electrochemical effects has been modelled (Knight and Endres 1990). A comparison between experimental and theoretical dielectric constants and conductivities is shown in Fig. 2, for a frequency of 200 MHz (we observed that the influence of the frequency is negligible in the radio-frequency band). As can be appreciated, the comparison is satisfactory.

We obtain in this section the effective permittivity and conductivity as a function of the different fluid saturations for typical soils in a hydrocarbon spill, such as that represented in Fig. 1. We consider two contaminants (methanol and aviation gasoline) which have quite different values of dielectric constant. Table 1 gives the material properties of the single constituents, with the values corresponding to a frequency of 200 MHz. For water (Schön 1996)

$$\epsilon_{\mathrm{w}}^{0} = 80.1\epsilon_0, \qquad \epsilon_{\mathrm{w}}^{\infty} = 4.23\epsilon_0, \qquad \tau_{\mathrm{w}} = 9.3\,\mathrm{ps}, \qquad q = 0.987;$$

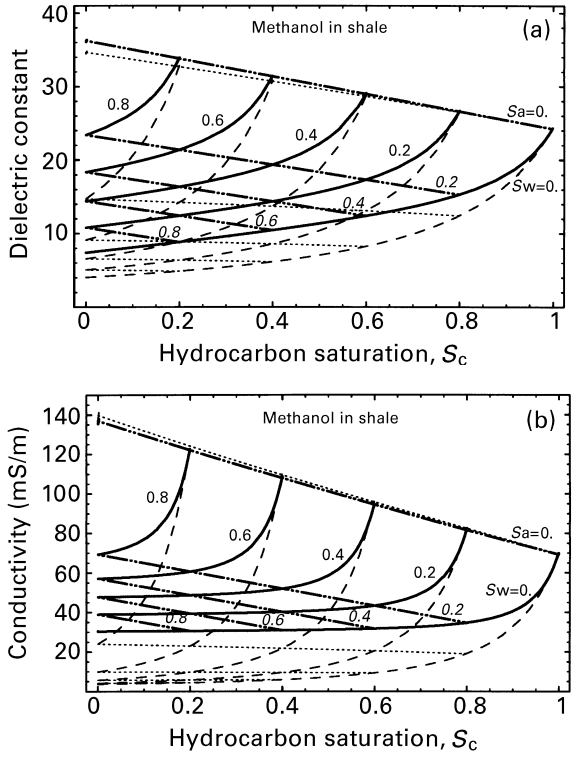

Figure 5. (a) Effective permittivities and (b) effective conductivities for shale partially saturated with methanol, water and air vs. methanol saturation. The thick continuous and broken lines correspond to the tangential (T) component and the thin broken and dotted lines correspond to the normal (N) component.

and for the clay/silt matrix

$$\epsilon_{cs}^0 = 20\epsilon_0, \qquad \epsilon_{cs}^\infty = 15\epsilon_0, \qquad \tau_{cs} = 9\,\text{ps}, \qquad q = 0.9.$$

The values indicated in Table 1 correspond to the static permittivity.

We consider a soil with a porosity equal to 0.4, i.e. $\phi = \phi_a + \phi_w + \phi_c = 0.4$. The respective saturations are given by

$$S_a = \frac{\phi_a}{\phi}, \quad S_w = \frac{\phi_w}{\phi}, \quad S_c = \frac{\phi_c}{\phi}.$$

Figures 3a and b show $\text{Re}(\epsilon)$ and $\omega\text{Im}(\epsilon)$, respectively, for sand partially saturated with methanol, water and air. The thick continuous lines correspond to constant water saturation (roman numbers) while the thick broken lines correspond to constant air saturation (italic numbers). For comparison, the thin dotted and broken lines show the curves for the CRIM model (see Appendix A). For instance, if $S_c = 0.4$ and $S_w = 0.4$, $S_a = 1 - S_w - S_c = 0.2$, giving an effective dielectric constant equal to $14\epsilon_0$. Soil fully

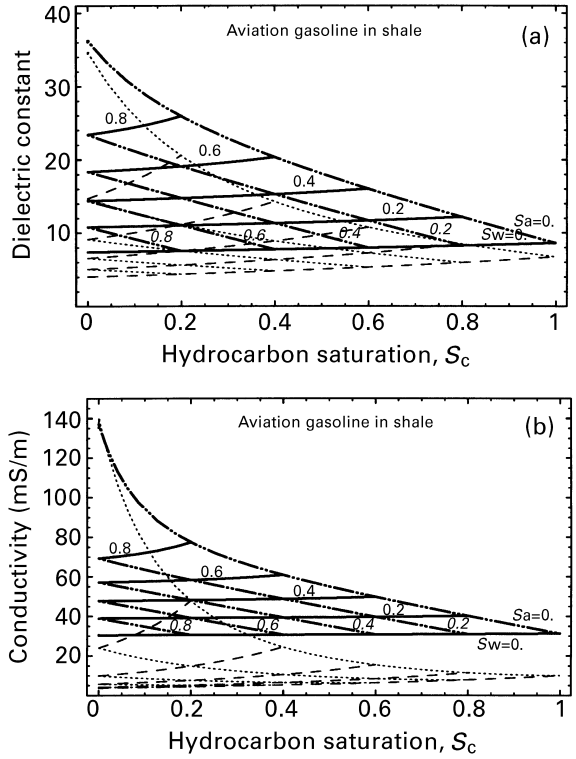

Figure 6. (a) Effective permittivities and (b) effective conductivities for shale partially saturated with aviation gasoline, water and air vs. gasoline saturation. The thick continuous and broken lines correspond to the tangential (T) component and the thin broken and dotted lines correspond to the normal (N) component.

saturated with water ($S_w = 1$) has a permittivity of $25\epsilon_0$; full air saturation corresponds to $S_w = S_c = 0$, with a permittivity of $2.7\epsilon_0$ (the lower value of the curve $S_w = 0$); full methanol saturation, i.e. $S_c = 1$, implies a permittivity of nearly $11\epsilon_0$ (the higher value of the curve $S_w = 0$). For a given water saturation, the dielectric constant increases with increasing methanol saturation, since methanol has a much higher permittivity than air. The same argument holds for the effective conductivity. This effect is more pronounced for increasing water content, since water at 200 MHz has a much higher permittivity than methanol ($78\epsilon_0$ vs. $31\epsilon_0$). The effective permittivity and conductivity for the sand partially saturated with aviation gasoline is shown in Fig. 4. Since aviation gasoline has a low permittivity value, the variation of the effective permittivity with increasing gasoline saturation is relatively small. Sand saturated with methanol has a higher permittivity than sand saturated with gasoline.

The effective permittivities $\epsilon_{T,\mathrm{eff}}$ and $\epsilon_{N,\mathrm{eff}}$ and the effective conductivities $\sigma_{T,\mathrm{eff}}$ and $\sigma_{N,\mathrm{eff}}$, for shale partially saturated with methanol, are plotted in Figs 5a and b, respectively. The connectivity parameter δ is taken as 0.3. As can be appreciated, the

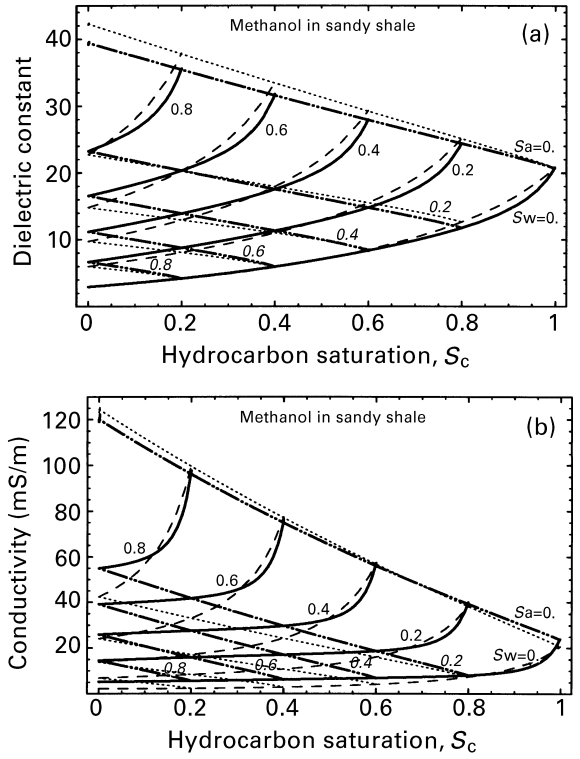

Figure 7. (a) Effective permittivities and (b) effective conductivities for sandy shale partially saturated with methanol, water and air vs. methanol saturation. Equal proportions of quartz and clay/silt are assumed. The thick continuous and broken lines correspond to the tangential (T) component and the thin broken and dotted lines correspond to the normal (N) component.

normal (N) components are lower than the tangential (T) components. However, note from (C14) that the electromagnetic properties along the horizontal (x, y-plane) and vertical (any plane containing the z-axis) directions are determined by ϵ_N and ϵ_T, respectively. This means that, according to Fig. 5, the vertical velocity is greater than the horizontal velocity. The maximum anisotropy occurs for $S_c = 0$, while in the absence of air, the soil is isotropic in practice. Moreover, the electromagnetic properties increase for increasing methanol and water saturations. On the other hand, shale saturated with aviation gasoline presents different characteristics, since the medium is anisotropic for all saturations (see Fig. 6).

The properties of a sandy shale saturated with methanol and aviation gasoline are shown in Figs 7 and 8, respectively. We consider equal proportions of sand and clay/silt, i.e. $\phi_q = \phi_{cs} = 0.3$, or $P = 0.5$. The presence of quartz (sand) makes the medium less anisotropic, and in this case, normal (N) components are higher than the tangential (T) components for certain hydrocarbon saturations.

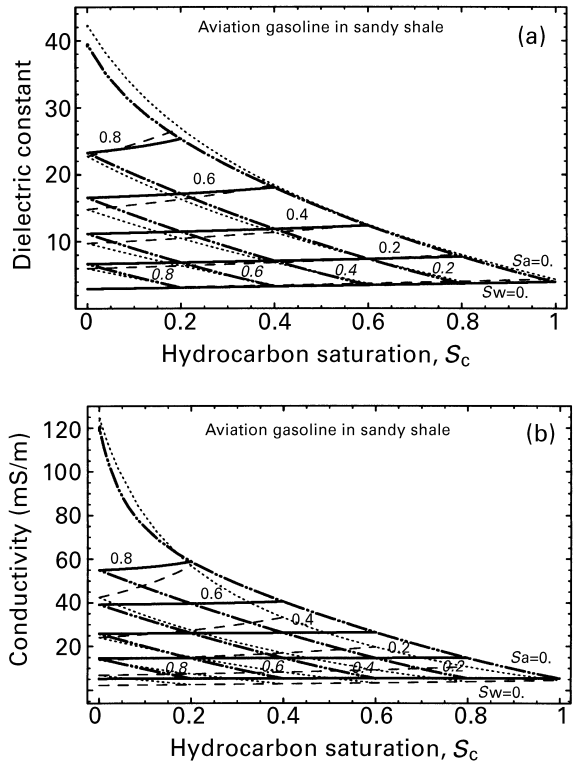

Figure 8. (a) Effective permittivities and (b) effective conductivities for sandy shale partially saturated with aviation gasoline, water and air vs. aviation gasoline and water saturations. Equal proportions of quartz and clay/silt are assumed. The thick continuous and broken lines correspond to the tangential (T) component and the thin broken and dotted lines correspond to the normal (N) component.

Finally, Fig. 9 shows polar representation of (a) the slowness, (b) the attenuation factor, (c) the energy velocity and (d) the quality factor, corresponding to the extraordinary wave (see Appendix C). The medium is the diffusion zone partially saturated with aviation gasoline, constituting part of the hydrocarbon spill in Fig. 1 (see also Table 2), and the frequency is 200 MHz. As mentioned above, the properties along the z-axis are determined by ϵ_T, and ϵ_N determines the properties along the x-axis. This fact explains the anisotropic characteristics of the medium, based on the permittivity and conductivity values indicated in Table 2.

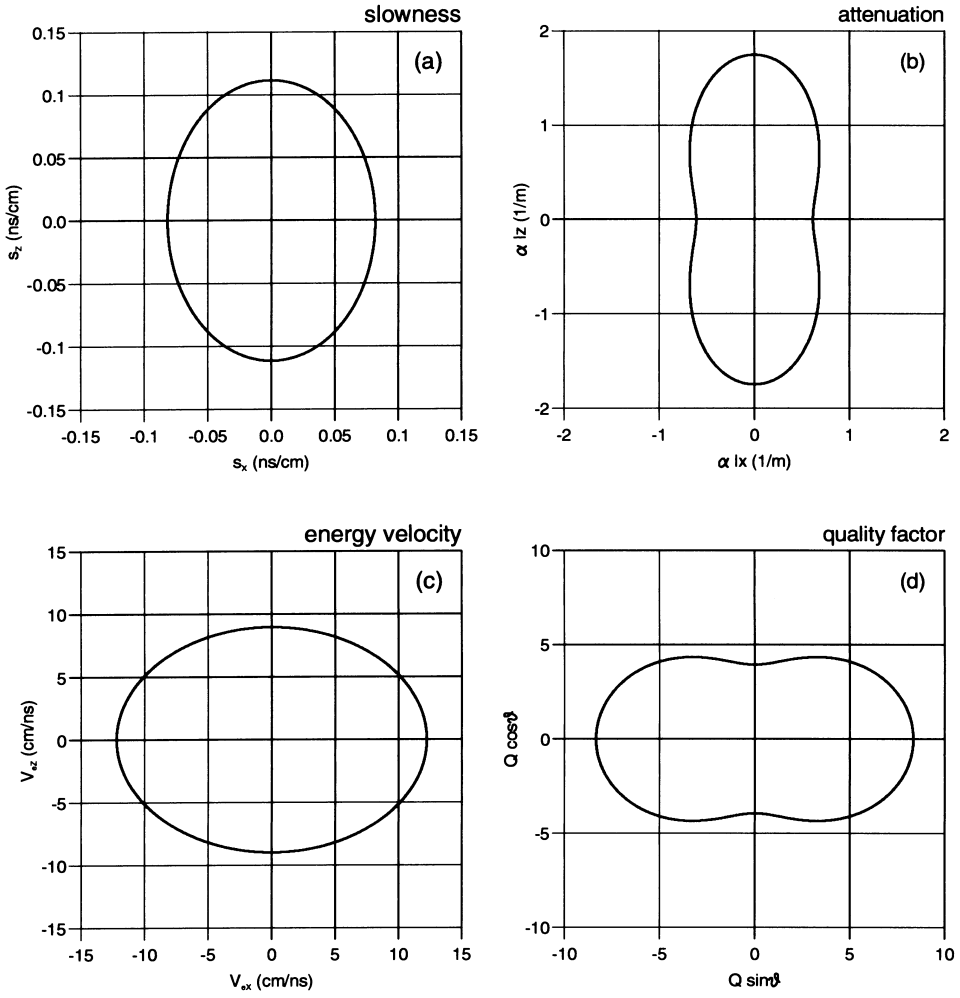

Figure 9. Polar representation of (a) the slowness, (b) the attenuation factor, (c) the energy velocity and (d) the quality factor for the medium constituting the diffusion zone in Fig. 1 (see also Table 2). The plots correspond to aviation gasoline.

Table 2. Properties of the hydrocarbon spill model.

Medium	ϕ_q	ϕ_{cs}	ϕ	S_w	S_a	S_c	$\epsilon_{T,eff}$ (ϵ_0)	$\epsilon_{N,eff}$ (ϵ_0)	$\sigma_{T,eff}$ (mS/m)	$\sigma_{N,eff}$ (mS/m)
Unsaturated zone*	0.6	0	0.4	0.3	0.7	0	7	7	0.4	0.4
Gaseous zone*	0.6	0	0.4	0.1	0.8	0.1	5(4)	5(4)	0.1	0.1
Capillary fringe*	0.6	0	0.4	0.3	0.1	0.6	14(7)	14(7)	0.6(0.4)	0.6(0.4)
Product core*	0.6	0	0.4	0.2	0	0.8	14(6)	14(6)	0.4(0.25)	0.4(0.25)
Diffusion zone†	0.4	0.3	0.3	0.4	0	0.6	18(11)	16(6)	40(31)	41(8)
Saturated zone†	0.4	0.3	0.3	1.0	0	0	24	21	73	73

Values in parentheses correspond to aviation gasoline.
* saturated with rain water; † saturated with salt water.

Numerical modelling application

Ground-penetrating radar can be used to locate hydrocarbon spills. The principal properties of hydrocarbons that may be detectable are the effective electromagnetic parameters given in (16) and (17). However, these properties are frequency dependent. Hence, the corresponding time-domain constitutive equations have a convolutional form. Strictly, such a general medium can be modelled by a set of Debye mechanisms, and the convolutions can be avoided by introducing hidden

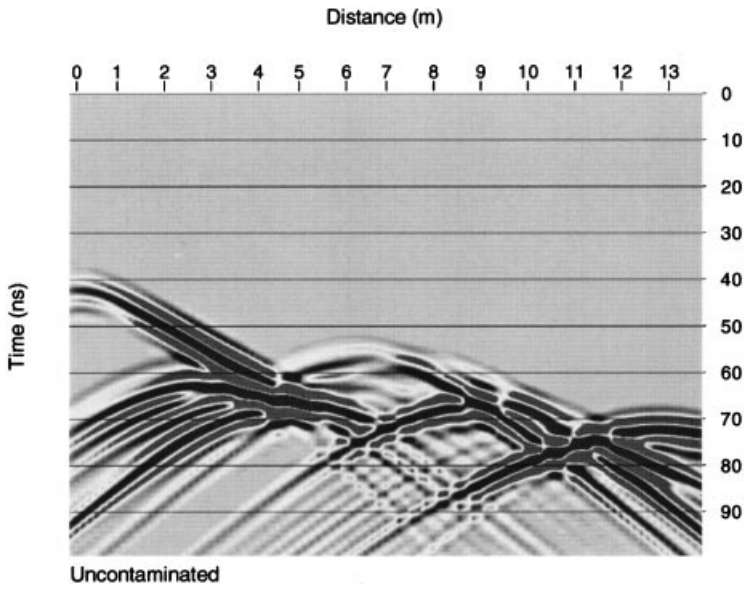

Figure 10. Radargram of the magnetic field in the absence of contaminants. In this case, the gaseous zone and the capillary fringe have the same properties as the unsaturated zone, and the product and the diffusion zones have the same properties as the saturated zone (see Fig. 1 and Table 2).

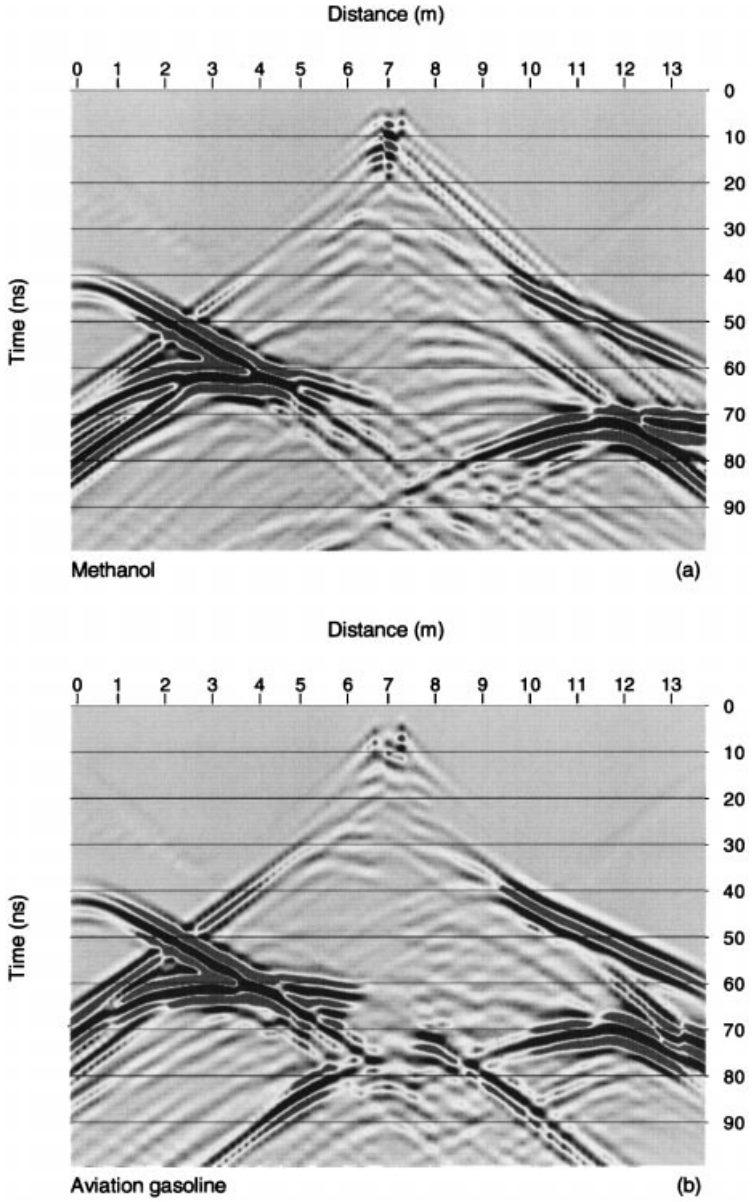

Figure 11. Radargram of the magnetic field corresponding to the hydrocarbon spill shown in Fig. 1, when the contaminant is (a) methanol and (b) aviation gasoline (see Tables 1 and 2).

variables (Carcione 1996a,b). Here, we compute the effective properties of the model shown in Fig. 1 at the central frequency of the transmitting antenna, and assume them to be frequency independent. We then assume that the anisotropic TM (transverse-magnetic) Maxwell equations can be expressed as

$$\begin{aligned} &\partial_x E_z - \partial_z E_x = \mu_0 \partial_t H_y + m_y, \\ &-\partial_z H_y = \sigma_{\mathrm{T,eff}} E_x + \epsilon_{\mathrm{T,eff}} \partial_t E_x + j_x, \\ &\partial_x H_y = \sigma_{\mathrm{N,eff}} E_z + \epsilon_{\mathrm{N,eff}} \partial_t E_z + j_z, \end{aligned} \tag{19}$$

where E_x, E_z, H_y are field components, m_y, j_x and j_z are external sources and μ_0 is the magnetic permeability of a vacuum. Table 2 yields the properties of the different soils composing the hydrocarbon spill (Fig. 1) at 200 MHz. The values correspond to methanol, and those in parentheses to aviation gasoline. The solid fractions and fluid saturations have been inferred from cores obtained at a contaminated site near an oil refinery.

We assume that above the water table the soils are partially saturated with rain water.

The numerical mesh has $N_X = 225$ and $N_Z = 125$ gridpoints, with a grid spacing $D_X = D_Z = 7.5$ cm. The source is a Ricker-type wavelet with a central frequency of 200 MHz, applied as a j_x 'plane-wave' in order to simulate a stacked radargram. The algorithm, similar to that developed by Carcione (1996a), uses a time step of 0.05 ns. Figure 10 represents a radargram of the magnetic field in the absence of contaminant. In this case, the gaseous zone and the capillary fringe have the same properties as the unsaturated zone, and the product and the diffusion zones have the same properties as the saturated zone. On the other hand, Fig. 11 shows the magnetic field corresponding to the hydrocarbon spill, when the contaminant is (a) methanol and (b) aviation gasoline. There is a correlation between the decreased signal amplitude and the presence of hydrocarbons, as observed by Daniels *et al.* (1995) in their experiments. This is explained by the lower plane-wave reflection coefficients of hydrocarbon-saturated soils as compared with reflections from the water table. It is clear that the GPR technique is sensitive to the presence of hydrocarbons, and distinguishes between them.

Conclusions

The magnitudes of the complex permittivity of soils saturated with air, water and hydrocarbons show significant variations, depending on the degree of saturation by the different fluids. This feature allows the use of high-frequency electromagnetic techniques, such as GPR, for detecting and mapping pools of near-surface low-loss contaminants. We consider two hydrocarbons, methanol and aviation gasoline, which have dissimilar dielectric constants. A soil saturated with methanol has a higher permittivity than that saturated with gasoline. For constant water saturation, the permittivity increases for increasing methanol saturation, while the variation is small when the soil contains aviation gasoline. If the soil is shaly, it exhibits anisotropic

properties with the vertical velocity being greater than the horizontal velocity, and the maximum anisotropy generally takes place in the absence of hydrocarbons. In particular, a shale fully saturated with methanol is isotropic, for practical purposes.

The use of a full-wave modelling method allows the computation of radargrams for a typical hydrocarbon spill, simulating the capillary fringe, the gaseous and diffusion zones, and the product core located on the water table. The modelling indicates that there is a decrease in reflection amplitude above the contaminant pool, as a consequence of the lower permittivity of the hydrocarbons with respect to water. Moreover, a methanol pool can be distinguished from an aviation gasoline pool in terms of the different electromagnetic reflection responses. The constitutive equations, tested with experimental data, and the simulation algorithm constitute a forward-modelling tool for aiding in the interpretation of hydrocarbon-contaminated soils.

Acknowledgements

This work was financed in part by the European Union under the INCO-COPERNICUS project 'Detection of Hydrocarbon Contaminated Soils by Electromagnetic Techniques', Contract Nr. ERBIC15CT960801. We are indebted to Fabio Cavallini for his helpful comments and criticism throughout the writing of this paper.

Appendix A

Dielectric properties of a partially saturated rock

A number of models have been proposed to determine the electromagnetic properties of composites. One such model, the complex refractive index method (CRIM) (e.g. Knight and Endres 1990), states that

$$\epsilon = \left(\sum_{\alpha} \gamma_{\alpha} \sqrt{\epsilon_{\alpha}} \right)^2, \tag{A1}$$

where γ_α and ϵ_α are the volume fraction and permittivity of the α phase. This model is very simple and easy to implement, but it has no rigorous theoretical foundation.

Here we propose a self-similar model, based on physical grounds, for calculating the complex permittivity of a soil saturated with many fluids. According to the self-consistent approximation (Sen *et al.* 1981; Feng and Sen 1985), the permittivity ϵ satisfies

$$0 = \sum_{\alpha} \gamma_{\alpha} \frac{\epsilon - \epsilon_{\alpha}}{2\epsilon + \epsilon_{\alpha}}, \tag{A2}$$

where γ_α and ϵ_α are the volume fraction and permittivity of the α phase. As Feng and Sen (1985) point out, a water-wet rock that remains percolating for small values of the porosity can be obtained from the assumption that water is the starting host material into which infinitesimal amounts of spheres of matrix and fluids are gradually

introduced. This model is in agreement with Archie's law, i.e. it preserves the continuity of the water phase.

According to (A2), the change $d\epsilon$ in ϵ due to a volume change dv_k caused by k spherical inclusions ($k=1,\ldots,N$) is given by

$$\frac{d\epsilon}{3\epsilon}=\sum_k \frac{dv_k}{v_w+\sum_l v_l}\left(\frac{\epsilon_k-\epsilon}{\epsilon_k+2\epsilon}\right). \tag{A3}$$

Let us assume that v_1 is the matrix volume, and that during the mixing process we keep constant the respective proportions. Then,

$$\frac{dv_k}{dv_1}=\frac{v_k}{v_1}=\frac{\gamma_k}{\gamma_1}\equiv\eta_k. \tag{A4}$$

The volume fraction of the matrix grains is

$$\psi=\frac{v_1}{v_w+\sum_l v_l}=\frac{v_1}{v_w+v_1\sum_l \eta_l}, \tag{A5}$$

where (A4) has been used. Differentiating (A5) gives

$$d\psi=(1-\psi\sum_l \eta_l)\frac{dv_1}{v_w+\sum_l v_l}. \tag{A6}$$

Substituting (A4) and (A5) into (A3) yields

$$\frac{d\epsilon}{3\epsilon}=\sum_k \frac{\eta_k d\psi}{1-\psi\sum_l \eta_l}\left(\frac{\epsilon_k-\epsilon}{\epsilon_k+2\epsilon}\right). \tag{A7}$$

Rearranging terms gives

$$\frac{d\epsilon}{3\epsilon}\left(\sum_k \eta_k\frac{\epsilon_k-\epsilon}{\epsilon_k+2\epsilon}\right)^{-1}=\frac{d\psi}{1-\psi\sum_l \eta_l}. \tag{A8}$$

In order to obtain the permittivity of the composite, (A8) must be integrated from $\psi=0$ to $\psi=\gamma_1$ with the condition $\epsilon=\epsilon_w$ for $\psi=0$. For two constituents, say quartz and water, the solution is given by (3), which reduces to

$$\left(\frac{\epsilon_q-\epsilon}{\epsilon_q-\epsilon_w}\right)\left(\frac{\epsilon_w}{\epsilon}\right)^{1/3}=\phi, \tag{A9}$$

where ϕ is the rock porosity. Alternatively

$$(1-\hat{\epsilon})^3=a\hat{\epsilon}, \tag{A10}$$

where

$$\hat{\epsilon}=\epsilon/\epsilon_q, \qquad a=\frac{\epsilon_q}{\epsilon_w}\left(1-\frac{\epsilon_w}{\epsilon_q}\right)^3\phi^3. \tag{A11}$$

This equation has the following solutions

$$\hat{\epsilon}_1 = 1 - \left(\frac{a}{3}\right)^{1/3}\left[\left(\frac{2a}{\gamma}\right)^{1/3} - \left(\frac{\gamma}{6}\right)^{1/3}\right],$$

$$\hat{\epsilon}_2 = 1 + \left(\frac{a}{12}\right)^{1/3}\left[z_0\left(\frac{a}{\gamma}\right)^{1/3} - z_0^*\left(\frac{\gamma}{12}\right)^{1/3}\right],$$

$$\hat{\epsilon}_3 = 1 + \left(\frac{a}{12}\right)^{1/3}\left[z_0^*\left(\frac{a}{\gamma}\right)^{1/3} - z_0\left(\frac{\gamma}{12}\right)^{1/3}\right], \tag{A12}$$

where

$$\gamma = \sqrt{3}(27 + 4a)^{1/2} - 9, \qquad z_0 = 1 + \mathrm{i}\sqrt{3}.$$

The physical solution is that approaching ϵ_w in the limit $\phi \rightarrow 1$.

For N constituents, the solution has the form

$$\left(\frac{\epsilon_w}{\epsilon}\right)^{1/3}\prod_i\left(\frac{\epsilon_w - r_i}{\epsilon - r_i}\right)^{s_i} = \phi, \tag{A13}$$

where the coefficients r_i and s_i are obtained by expanding the left-hand side of equation (A8) as

$$\frac{1}{3\epsilon}\left(\sum_k \eta_k \frac{\epsilon_k - \epsilon}{\epsilon_k + 2\epsilon}\right)^{-1} = \frac{1}{\chi}\left[\frac{1}{3\epsilon} + \frac{p(\epsilon)}{q(\epsilon)}\right], \tag{A14}$$

where $\chi = \sum_l \eta_l$, and $p(\epsilon)$ and $q(\epsilon)$ are polynomials. Then, r_i are the roots of $q(\epsilon)$ and $s_i = s(r_i)$ with

$$s(\epsilon) = p(\epsilon)\left(\frac{\mathrm{d}q}{\mathrm{d}\epsilon}\right)^{-1}. \tag{A15}$$

For $N = 3$, $\chi = 1 + \eta_2$ and the polynomials are

$$p(\epsilon) = 2\chi\epsilon + \epsilon_2 + \epsilon_1\eta_2, \tag{A16}$$

$$q(\epsilon) = -2\chi\epsilon^2 + [\epsilon_1(2 - \eta_2) - \epsilon_2(1 - 2\eta_2)]\epsilon + \epsilon_1\epsilon_2\chi. \tag{A17}$$

For $N = 4$, $\chi = 1 + \eta_2 + \eta_3$ and

$$\begin{aligned} p(\epsilon) = {} & 4\chi\epsilon^2 + 2[\epsilon_1(\eta_2 + \eta_3) + \epsilon_2(1 + \eta_3) + \epsilon_3(1 + \eta_2)]\epsilon \\ & + \epsilon_1\epsilon_3\eta_2 + \epsilon_2\epsilon_3 + \epsilon_1\epsilon_2\eta_3, \end{aligned} \tag{A18}$$

$$\begin{aligned} q(\epsilon) = {} & -4\chi\epsilon^3 - 2[\epsilon_1(-2 + \eta_2 + \eta_3) + \epsilon_2(1 - 2\eta_2 + \eta_3) + \epsilon_3(1 + \eta_2 - 2\eta_3)]\epsilon^2 \\ & + [\epsilon_2\epsilon_3(-1 + 2\eta_2 + 2\eta_3) + \epsilon_1\epsilon_2(2 + 2\eta_2 - \eta_3) + \epsilon_1\epsilon_3(2 - \eta_2 + 2\eta_3)]\epsilon \\ & + \epsilon_1\epsilon_2\epsilon_3\chi \quad . \end{aligned} \tag{A19}$$

The solution of the non-linear equation (A13) in the complex plane can be easily

computed using any complex-root-finder algorithm, initialized, for instance, with the values obtained by the CRIM formula.

Appendix B

Properties of a finely layered medium

Let us consider a layered medium, where each layer is homogeneous (but anisotropic) and thin compared with the wavelength of the electromagnetic wave. If the layer interfaces are parallel to the (x, z)-plane, we express the constitutive equation of each layer as

$$\mathbf{J} = \begin{pmatrix} \mathbf{J}_{\mathrm{T}} \\ J_{\mathrm{N}} \end{pmatrix} = \begin{pmatrix} \boldsymbol{\sigma}_{\mathrm{TT}} & \boldsymbol{\sigma}_{\mathrm{TN}} \\ \boldsymbol{\sigma}_{\mathrm{NT}}^{\top} & \sigma_{\mathrm{NN}} \end{pmatrix} \cdot \begin{pmatrix} \mathbf{E}_{\mathrm{T}} \\ E_{\mathrm{N}} \end{pmatrix}, \tag{B1}$$

where

$$\mathbf{J}_{\mathrm{T}}^{\top} = [J_x, J_y], \qquad J_{\mathrm{N}} = J_z$$

$$\mathbf{E}_{\mathrm{T}}^{\top} = [E_x, E_y], \qquad E_{\mathrm{N}} = E_z,$$

$$\boldsymbol{\sigma}_{\mathrm{TT}} = \begin{pmatrix} \sigma_{11} & \sigma_{12} \\ \sigma_{21} & \sigma_{22} \end{pmatrix}, \qquad \sigma_{\mathrm{NN}} = \sigma_{33},$$

$$\boldsymbol{\sigma}_{\mathrm{TN}}^{\top} = [\sigma_{13}, \sigma_{23}], \qquad \boldsymbol{\sigma}_{\mathrm{NT}}^{\top} = [\sigma_{31}, \sigma_{32}].$$

The boundary conditions at the interfaces ($\mathbf{E}_{\mathrm{T}}$ and J_{N} are continuous) imply that $\mathbf{E}_{\mathrm{T}}$ and J_{N} vary very slowly. On the contrary, $\mathbf{J}_{\mathrm{T}}$ and E_{N} vary rapidly from layer to layer.

For isotropic layers

$$\boldsymbol{\sigma}_{\mathrm{TT}} = \begin{pmatrix} \sigma & 0 \\ 0 & \sigma \end{pmatrix}, \qquad \sigma_{\mathrm{NN}} = \sigma,$$

$$\boldsymbol{\sigma}_{\mathrm{TN}}^{\top} = \boldsymbol{\sigma}_{\mathrm{NT}}^{\top} = [0, 0].$$

Following Davydycheva, Druskin and Habashy (1996), we express the rapidly varying transverse components of the current ($\mathbf{J}_{\mathrm{T}}$) and the normal component of the electric field (E_{N}) in terms of the slowly varying transverse components of the electric field ($\mathbf{E}_{\mathrm{T}}$) and the normal component of the current (J_{N}). After averaging we obtain

$$\langle E_{\mathrm{N}} \rangle = \langle \sigma_{\mathrm{NN}}^{-1} \rangle J_{\mathrm{N}}, \qquad \langle \mathbf{J}_{\mathrm{T}} \rangle = \langle \boldsymbol{\sigma}_{\mathrm{TT}} \rangle \cdot \mathbf{E}_{\mathrm{T}},$$

where $\langle \cdot \rangle$ is the weighted averaging operator. Expressing the average current in terms of the averaged electric fields gives

$$\mathbf{J} = \begin{pmatrix} \langle \mathbf{J}_{\mathrm{T}} \rangle \\ J_{\mathrm{N}} \end{pmatrix} = \begin{pmatrix} \langle \boldsymbol{\sigma}_{\mathrm{TT}} \rangle & 0 \\ 0 & \langle \sigma_{\mathrm{NN}}^{-1} \rangle^{-1} \end{pmatrix} \cdot \begin{pmatrix} \mathbf{E}_{\mathrm{T}} \\ \langle E_{\mathrm{N}} \rangle \end{pmatrix}. \tag{B2}$$

In the case of anisotropic layers, the constitutive relationship of the composite is

$$\langle \mathbf{J} \rangle = \boldsymbol{\Sigma} \cdot \langle \mathbf{E} \rangle$$

or

$$\begin{pmatrix} \langle \mathbf{J}_{\mathrm{T}} \rangle \\ J_{\mathrm{N}} \end{pmatrix} = \begin{pmatrix} \boldsymbol{\Sigma}_{\mathrm{TT}} & \boldsymbol{\Sigma}_{\mathrm{TN}} \\ \boldsymbol{\Sigma}_{\mathrm{NT}}^{\top} & \Sigma_{\mathrm{NN}} \end{pmatrix} \cdot \begin{pmatrix} \mathbf{E}_{\mathrm{T}} \\ \langle E_{\mathrm{N}} \rangle \end{pmatrix},$$

where

$$\boldsymbol{\Sigma}_{\mathrm{TT}} = \langle \boldsymbol{\sigma}_{\mathrm{TT}} \rangle - \langle \sigma_{\mathrm{TN}} \sigma_{\mathrm{NN}}^{-1} \sigma_{\mathrm{NT}}^{\top} \rangle + \langle \sigma_{\mathrm{TN}} \sigma_{\mathrm{NN}}^{-1} \rangle \langle \sigma_{\mathrm{NN}}^{-1} \rangle^{-1} \langle \sigma_{\mathrm{NN}}^{-1} \sigma_{\mathrm{NT}}^{\top} \rangle,$$

$$\boldsymbol{\Sigma}_{\mathrm{TN}} = \langle \sigma_{\mathrm{TN}} \sigma_{\mathrm{NN}}^{-1} \rangle \langle \sigma_{\mathrm{NN}}^{-1} \rangle^{-1},$$

$$\boldsymbol{\Sigma}_{\mathrm{NT}} = \langle \sigma_{\mathrm{NN}}^{-1} \rangle^{-1} \langle \sigma_{\mathrm{NN}}^{-1} \sigma_{\mathrm{NT}} \rangle,$$

$$\Sigma_{\mathrm{NN}} = \langle \sigma_{\mathrm{NN}}^{-1} \rangle^{-1}.$$

Appendix C

Plane-wave analysis

Let us denote the general permittivity matrix of the composite by

$$\boldsymbol{\epsilon} = \begin{pmatrix} \epsilon_{\mathrm{T}} & 0 & 0 \\ 0 & \epsilon_{\mathrm{T}} & 0 \\ 0 & 0 & \epsilon_{\mathrm{N}} \end{pmatrix}. \tag{C1}$$

Assume *non-uniform* plane waves with a phase factor

$$\exp[\mathrm{i}\omega(\boldsymbol{\xi} \cdot \mathbf{x} - t)], \tag{C2}$$

where $\boldsymbol{\xi}$, the complex slowness vector, is equivalent to $\mathbf{k}/\omega$, with $\mathbf{k}$ and ω being the wavenumber vector and frequency, respectively. Note that

$$\nabla \times \rightarrow \mathrm{i}\omega \boldsymbol{\xi} \times \quad \text{and} \quad \partial/\partial t \rightarrow -\mathrm{i}\omega, \tag{C3}$$

where $\times$ denotes the vector product.

Maxwell's equations for a plane wave of the form (C2) read

$$\boldsymbol{\xi} \times \mathbf{E} = \mu \mathbf{H}, \tag{C4}$$

$$\boldsymbol{\xi} \times \mathbf{H} = -\boldsymbol{\epsilon} \cdot \mathbf{E}, \tag{C5}$$

(Chew 1990), where μ is the magnetic permeability and $\mathbf{H}$ is the magnetic field. Taking the vector product of (C4) with $\boldsymbol{\xi}$ and using (C5) gives

$$\mu \boldsymbol{\xi} \times (\boldsymbol{\xi} \times \mathbf{E}) + \boldsymbol{\epsilon} \cdot \mathbf{E} = 0, \tag{C6}$$

for three equations in the components of $\mathbf{E}$.

Let us consider the transversely isotropic case given by (C1). Equation (C6) can be expressed as

$$\boldsymbol{\Gamma} \cdot \mathbf{E} = \mathbf{0}, \tag{C7}$$

where

$$\mathbf{\Gamma} = \mu^{-1}\begin{pmatrix} \mu\epsilon_{\mathrm{T}} - (\xi_2^2 + \xi_3^2) & \xi_1\xi_2 & \xi_1\xi_3 \\ \xi_1\xi_2 & \mu\epsilon_{\mathrm{T}} - (\xi_1^2 + \xi_3^2) & \xi_2\xi_3 \\ \xi_1\xi_3 & \xi_2\xi_3 & \mu\epsilon_{\mathrm{N}} - (\xi_1^2 + \xi_2^2) \end{pmatrix}. \tag{C8}$$

The vanishing of the determinant yields a factorizable dispersion relationship:

$$[(\mu\epsilon_{\mathrm{T}} - \xi_3^2)(\mu\epsilon_{\mathrm{N}} - \xi_{\mathrm{T}}^2) - \xi_{\mathrm{T}}^2\xi_3^2](\mu\epsilon_{\mathrm{T}} - \xi^2) = 0, \tag{C9}$$

where $\xi_{\mathrm{T}}^2 = \xi_1^2 + \xi_2^2$ and $\xi^2 = \xi_{\mathrm{T}}^2 + \xi_3^2$ give the complex slowness. These factors give the slowness sections indicated in Fig. 12, with solutions

$$\xi^2 = \mu\epsilon_{\mathrm{T}} \quad \text{and} \quad \frac{\xi_{\mathrm{T}}^2}{\mu\epsilon_{\mathrm{N}}} + \frac{\xi_3^2}{\mu\epsilon_{\mathrm{T}}} = 1, \tag{C10}$$

corresponding to spherical and ellipsoidal complex slownesses, respectively. The type of mode is indicated in Fig. 12. In the TM (TE) case, the magnetic (electric) field vector is normal to the propagation plane.

Slowness, phase velocity and attenuation

The slowness vector can be split into real and imaginary vectors such that

$$\omega\mathrm{Re}(\boldsymbol{\xi}\cdot\mathbf{x} - t)$$

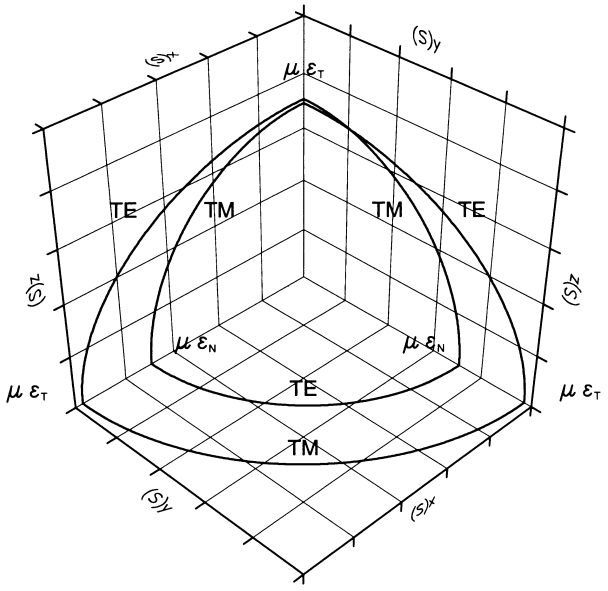

Figure 12. Intersection of the slowness surface with the principal planes. The corresponding waves are either transverse electric (TE) or transverse magnetic (TM). The values on the axes refer to the square of the complex slowness.

is the phase and

$$-\omega \mathrm{Im}(\boldsymbol{\xi} \cdot \mathbf{x})$$

is the attenuation. Let us assume that propagation and attenuation directions coincide. This is a *uniform* plane wave, the equivalent of a homogeneous plane wave in viscoelasticity. The slowness vector can be expressed as

$$\boldsymbol{\xi} = \xi(l_1, l_2, l_3)^{\top} = \xi \hat{\boldsymbol{\xi}}, \tag{C11}$$

where $\hat{\boldsymbol{\xi}}$ is a real unit vector, with l_i being the direction cosines. We obtain the real wavenumber vector and the real attenuation vector as

$$\mathrm{Re}(\boldsymbol{\xi}) \quad \text{and} \quad \boldsymbol{\alpha} = \omega \mathrm{Im}(\boldsymbol{\xi}), \tag{C12}$$

respectively.

Substituting (C11) into (C10) and defining the complex velocity $V \equiv \xi^{-1}$, the phase velocity and attenuation are

$$V_{\mathrm{p}} = [\mathrm{Re}(V^{-1})]^{-1} \quad \text{and} \quad \alpha = \omega \mathrm{Im}(V^{-1}), \tag{C13}$$

respectively, where

$$V = V_{\mathrm{o}} = (\mu \epsilon_{\mathrm{T}})^{-1/2} \quad \text{and} \quad V = V_{\mathrm{e}} = \left(\frac{l_{\mathrm{T}}^2}{\mu \epsilon_{\mathrm{N}}} + \frac{l_3^2}{\mu \epsilon_{\mathrm{T}}} \right)^{1/2} \tag{C14}$$

for the ordinary and the extraordinary waves, with $l_{\mathrm{T}}^2 = l_1^2 + l_2^2$.

Energy velocity, wavefront and quality factor

The scalar product of the complex conjugate of (C5) with $\mathbf{E}$, the use of the relationship

$$2\mathrm{Im}(\boldsymbol{\xi}) \cdot (\mathbf{E} \times \tilde{\mathbf{H}}) = (\boldsymbol{\xi} \times \mathbf{E}) \cdot \tilde{\mathbf{H}} + \mathbf{E} \cdot (\boldsymbol{\xi} \times \tilde{\mathbf{H}}) \tag{C17}$$

and substitution of (C4), gives Umov–Poynting's theorem for plane waves

$$\mathrm{Im}(\boldsymbol{\xi}) \cdot \mathbf{P} = \mathrm{i}(u_{\mathrm{e}} - u_{\mathrm{m}}), \tag{C15}$$

where

$$\mathbf{P} = \tfrac{1}{2} \mathbf{E} \times \tilde{\mathbf{H}} \tag{C16}$$

is the complex Umov–Poynting vector, and

$$u_{\mathrm{e}} = \tfrac{1}{4} \mathbf{E} \cdot (\boldsymbol{\epsilon} \cdot \tilde{\mathbf{E}}) \quad \text{and} \quad u_{\mathrm{m}} = \tfrac{1}{4} (\boldsymbol{\mu} \cdot \mathbf{H}) \cdot \tilde{\mathbf{H}} \tag{C17}$$

are the complex time-average electric and magnetic energy densities (a tilde above a variable denotes complex conjugate). The imaginary part of (C15) gives the balance of stored energy and the real part gives the balance of dissipated energy.

The energy velocity $\mathbf{V}_{\mathrm{en}}$ is given by the energy power flow $\mathrm{Re}(\mathbf{P})$ divided by the total stored energy $u_{\mathrm{s}} = \mathrm{Re}(u_{\mathrm{e}} + u_{\mathrm{m}})$,

$$\mathbf{V}_{\mathrm{en}} = \frac{\mathrm{Re}(\mathbf{P})}{\mathrm{Re}(u_{\mathrm{e}} + u_{\mathrm{s}})}. \tag{C18}$$

Let us consider the TM mode propagating in the (1,3)-plane. Then

$$\mathbf{H} = H_0[0, 1, 0]^\top \exp[\mathrm{i}(\boldsymbol{\xi} \cdot \mathbf{x})], \tag{C19}$$

where H_0 is a complex amplitude. By virtue of (C4),

$$\mathbf{E} = -\boldsymbol{\epsilon}^{-1} \cdot (\boldsymbol{\xi} \times \mathbf{H}) = H_0 \xi \left[\frac{l_3}{\epsilon_\mathrm{T}}, 0, \frac{-l_1}{\epsilon_\mathrm{N}}\right]^\top \exp[\mathrm{i}(\boldsymbol{\xi} \cdot \mathbf{x})], \tag{C20}$$

where we have assumed uniform plane waves. Substituting the electric and magnetic fields into the energy densities (C17) yields

$$u_\mathrm{e}^\mathrm{TM} = \tfrac{1}{4}\mu |H_0|^2 \frac{V_\mathrm{e}^2}{|V_\mathrm{e}|^2} \exp(-2\boldsymbol{\alpha} \cdot \mathbf{x}), \qquad u_m^\mathrm{TM} = \tfrac{1}{4}\mu |H_0|^2 \exp(-2\boldsymbol{\alpha} \cdot \mathbf{x}), \tag{C21}$$

where V_e is given in (C14). Summing the electric and magnetic energies and taking real parts gives the total stored energy,

$$u_\mathrm{s}^\mathrm{TM} = \tfrac{1}{2}\mu |H_0|^2 \mathrm{Re}\left(\frac{V_\mathrm{e}}{V_\mathrm{pe}}\right) \exp(-2\boldsymbol{\alpha} \cdot \mathbf{x}), \tag{C22}$$

where V_pe is the phase velocity of the extraordinary wave.

On the other hand, it is easy to show that the TM power flow vector is

$$\tfrac{1}{2}|H_0|^2 \mathrm{Re}\left[\frac{1}{V_\mathrm{e}}\left(\hat{\mathbf{e}}_1 \frac{l_1}{\epsilon_\mathrm{N}} + \hat{\mathbf{e}}_3 \frac{l_3}{\epsilon_\mathrm{T}}\right)\right] \exp(-2\boldsymbol{\alpha} \cdot \mathbf{x}). \tag{C23}$$

From (C21) and (C23) we obtain the energy velocity for TM waves propagating in the (1, 3)-plane.

$$\mathbf{V}_\mathrm{en}^\mathrm{TM} = \frac{V_\mathrm{pe}}{\mu \mathrm{Re}(V_\mathrm{e})}\left[\mathrm{Re}\left(\frac{l_1}{\epsilon_\mathrm{N} V_\mathrm{e}}\right)\hat{\mathbf{e}}_1 + \mathrm{Re}\left(\frac{l_3}{\epsilon_\mathrm{T} V_\mathrm{e}}\right)\hat{\mathbf{e}}_3\right]. \tag{C24}$$

Since there is rotational symmetry, (C24) gives the energy velocity across any vertical plane. The wavefront of the ordinary wave is isotropic and it can easily be shown that, in this case, the energy velocity equals the phase velocity.

The quality factor quantifies, in some way, energy dissipation in matter from the electric current standpoint. As stated by Harrington (1961, p. 28), the quality factor is defined as the magnitude of reactive current density to the magnitude of dissipative current density. In viscoelastodynamics, a common definition of quality factor is that it is twice the ratio between the average potential energy density and the dissipated energy density. Accordingly, and using the acoustic-electromagnetic analogy (Carcione and Cavallini 1995), the quality factor is defined here as twice the ratio between the average electric energy and the density of energy dissipated in one cycle:

$$Q = \frac{\mathrm{Re}(u_\mathrm{e})}{\mathrm{Im}(u_\mathrm{e})}. \tag{C25}$$

Using (C21), (C25) for the extraordinary wave becomes

$$Q_\mathrm{e} = \frac{\mathrm{Re}(V_\mathrm{e}^2)}{\mathrm{Im}(V_\mathrm{e}^2)}. \tag{C26}$$

For the ordinary wave, the quality factor takes the following simple form:

$$Q_{\mathrm{o}} = \frac{\mathrm{Re}(V_{\mathrm{o}}^2)}{\mathrm{Im}(V_{\mathrm{o}}^2)} = -\frac{\mathrm{Re}(\mu\epsilon_{\mathrm{T}})}{\mathrm{Im}(\mu\epsilon_{\mathrm{T}})}. \tag{C27}$$

For real magnetic permeability and using (16) and (17), (C27) becomes

$$Q_{\mathrm{o}} = \omega\frac{\epsilon_{\mathrm{T,eff}}}{\sigma_{\mathrm{T,eff}}}. \tag{C28}$$

The concept of the quality factor can be considered as a generalization of the concept of Q in circuit theory. Good dielectrics have high Q values, and conductors have very low Q values.

References

Archie G.E. 1942. The electrical resistivity log as an aid in determining some reservoir characteristics. *Transactions of the American Institute of Mining Engineers* **146**, 54–62.

Benson A.K. 1995. Applications of ground penetrating radar in assessing some geological hazards: examples of groundwater contamination, faults, cavities. *Journal of Applied Geophysics* **33**, 177–193.

Bergman D.J. 1978. The dielectric constant of a composite material – a problem in classical physics. *Physics Reports* **43**, 377–407.

Carcione J.M. 1996a. Ground-penetrating radar: wave theory and numerical simulation in lossy anisotropic media. *Geophysics* **61**, 1664–1677.

Carcione J.M. 1996b. Ground radar simulation for archaeological applications. *Geophysical Prospecting* **44**, 871–888.

Carcione J.M. and Cavallini F. 1995. On the acoustic-electromagnetic analogy. *Wave Motion* **21**, 149–162.

Chew W.C. 1990. *Waves and Fields in Inhomogeneous Media*. Van Nostrand Reinhold Co.

Cole K.S. and Cole R.H. 1941. Dispersion and absorption in dielectrics. *Journal of Chemical Physics* **9**, 341–351.

Daniels J.J., Roberts R. and Vendl M. 1995. Ground penetrating radar for the detection of liquid contaminants. *Journal of Applied Geophysics* **33**, 195–207.

Davydycheva S., Druskin V. and Habashy T.M. 1996. *Solution of Maxwell's equations in an arbitrary 3-D inhomogeneous anisotropic media with sharp discontinuities using a finite-difference scheme on a regular Cartesian grid with material averaging*. Schlumberger-Doll Research, Ridgefield, Report #EMG-002-96-15.

Endres A.L. and Redman D.J. 1993. Modeling the electrical properties of porous rocks and soils containing immiscible contaminants. *Proceedings of the Symposium on the Application of Geophysics to Engineering and Environmental Problems*, Englewood, Colorado, 21–38.

Feng S. and Sen P.N. 1985. Geometrical model of conductive and dielectric properties of partially saturated rocks. *Journal of Applied Physics* **58**, 3236–3243.

Greenhouse J., Brewster M., Schneider G., Redman D., Annan P., Olhoeft G. *et al.* 1993. Geophysics and solvents: the Borden experiment. *The Leading Edge* **12**, 261–267.

Grumman D.L. and Daniels J.J. 1995. Experiments on the detection of organic contaminants in the vadose zone. *Journal of Environmental and Engineering Geophysics* **0**, 31–38.

Harrington R.F. 1961. *Time-Harmonic Electromagnetic Fields*. McGraw-Hill Book Co.

Knight R. and Endres A. 1990. A new concept in modeling the dielectric response of sandstones: defining a wetted rock and bulk water system. *Geophysics* **55**, 586–594.

Nash M.S., Atekwana E. and Sauck W.A. 1997. Geophysical investigation of anomalous conductivity at a hydrocarbon contaminated site. *Proceedings of the Symposium on the Application of Geophysics to Engineering and Environmental Problems*, SAGEEP 97, Reno, Nevada (ed. R.S. Bell), **2**, 675–683.

Olhoeft G.R. 1987. *Electrical Properties from 10^{-3} to 10^{+9} Hz – Physics and Chemistry.* American Institute of Physics.

Schön J.H. 1996. *Physical Properties of Rocks, Handbook of Geophysical Exploration*. Pergamon Press, Inc.

Schwille F. 1967. Petroleum contamination of the subsoil – a hydrocarbon problem. In: *The Joint Problems of the Oil and Water Industries* (ed. P. Hepple), pp. 23–53. Elsevier Science Publishing Co.

Sen P.N., Scala C. and Cohen M.H. 1981. A self-similar model for sedimentary rocks with applications to the dielectric constant of fused glass beads. *Geophysics* **46**, 781–795.

Taherian M.R., Kenyon W.E. and Safinya K.A. 1990. Measurement of dielectric response of water-saturated rocks. *Geophysics* **55**, 1530–1541.

Vernik L. and Nur A. 1992. Ultrasonic velocity and anisotropy of hydrocarbon source rocks. *Geophysics* **57**, 727–735.

Von Hippel A.R. (ed.) 1961. *Dielectric Materials and Applications*. MIT Press, Cambridge, MA.

Whiteley B. 1997. Delineation of voided and hydrocarbon contaminated regions with RDEM and STI. *Proceedings of the Symposium on the Application of Geophysics to Engineering and Environmental Problems*, SAGEEP 97, Reno, Nevada (ed. R.S. Bell), **2**, 597–607.